Lawrence Berkeley National Laboratory

Title

Unveiling the Emergent Traits of Chiral Spin Textures in Magnetic Multilayers

Permalink

https://escholarship.org/uc/item/88j6z8zj

Journal

Advanced Science, 9(6)

ISSN

2198-3844

Authors

Chen, Xiaoye
Lin, Ming
Kong, Jian Feng
et al.

Publication Date

2022-02-01

DOI

10.1002/advs.202103978

Peer reviewed

Emergence of compact Néel skyrmion character from interfacial chiral interactions in multilayers

Xiaoye Chen,[1,2] Ming Lin,[1,*] Jian Feng Kong,[3,*] Hui Ru Tan,[1] Anthony K.C. Tan,[2] Soong-Geun Je,[4] Hang Khume Tan,[1,2] Khoong Hong Khoo,[3] Mi-Young Im,[4] and Anjan Soumyanarayanan[1,2,5,†]

[1]*Institute of Materials Research & Engineering, Agency for Science, Technology & Research (A*STAR), 138634 Singapore*

[2]*Data Storage Institute, Agency for Science, Technology & Research (A*STAR), 138634 Singapore*

[3]*Institute of High Performance Computing, Agency for Science, Technology & Research (A*STAR), 138632 Singapore*

[4]*Center for X-ray Optics, Lawrence Berkeley National Laboratory, Berkeley, California 94720, USA*

[5]*Physics Department, National University of Singapore (NUS), 117551 Singapore*

Magnetic skyrmions are topologically wound nanoscale textures of spins. Demonstrations of their room temperature stability and electrical manipulation in industry-friendly multilayer films have led to an explosion of research activities. However, several fundamental issues concerning multilayer skyrmions – including their domain wall structure, thermodynamic stability, formation mechanism, and crucially their distinction from well-studied "magnetic bubbles" – remain highly debated and experimentally unaddressed to date. Here we elucidate these skyrmion characteristics on a tunable multilayer platform – wherein the chiral interactions governing spin texture energetics can be varied over a wide range – using a combination of full-field electron and soft X-ray microscopies with numerical simulations. With increasing chiral interactions, we demonstrate the emergence of Néel helicity, followed by a transition from bubble to compact skyrmion character, and a change in the skyrmion formation mechanism. Together with our analytical model, these experiments establish a comprehensive microscopic framework for investigating and tailoring skyrmion character in multilayer films.

A. INTRODUCTION

A1. Seminal advances in tailoring interfacial interactions in thin magnetic films have led to the room temperature (RT) stabilization of nanoscale spin textures – most notably magnetic skyrmions[1–4]. In light of past efforts on magnetic bubbles and domain walls (DWs)[5–8], the excitement around magnetic skyrmions stems largely from three distinguishing characteristics. First, skyrmions possess non-trivial topology, which arises from material-specific chiral winding of spins around the centre – known as *helicity* – and enables electrical detection[9]. Second, they remain stable at sizes down to 2 nm[10,11]: a crucial attribute for ever-shrinking memory devices[12–14]. Finally, they can be electrically created from uniform or stripe domain states[15–18]: attractive for logic and computing applications[19–21]. While multilayer films offer a platform ripe for tailoring skyrmions at RT[4,22], a microscopic framework elucidating the emergence of these key skyrmionic attributes remains to be established.

A2. Much of the character of chiral magnetic textures can be related to a single material parameter, $\kappa = \pi D / 4\sqrt{AK_{\text{eff}}}$. Here D is the interfacial Dzyaloshinskii-Moriya interaction (DMI), which sets the DW chirality[23,24], A is the exchange stiffness and K_{eff} is the effective uniaxial anisotropy[25–28]. Notably, κ is non-zero only for fixed DW chirality ($D > 0$). Moreover, its magnitude characterizes DW stability relative to the uniform state, as the denominator ($4\sqrt{AK_{\text{eff}}}$) represents the energy cost, and numerator (πD) the energy saved in chiral DW formation[25,28]. As κ demarcates the DMI-dominated regime ($\kappa > 1$) from that governed by magnetostatic interactions ($\kappa \ll 1$), it is expected to dictate the formation, extent and stability of skyrmions[22,27,29].

A3. Aspects of skyrmion character have been individually explored in multilayer films using dedicated imaging techniques, prompting some debate. First, while some reports confirm their Néel helicity[3,30], others have reported a considerable Bloch component with a layer- and material-dependent magnitude[31,32]. Meanwhile, investigations of size and stability evolution have thus far been limited to two contrasting regimes due to material constraints. On one hand, the $\kappa > 1$ (high DMI) regime has been explored in epitaxial films at low temperatures, and yields small skyrmions[10,28,33]. Meanwhile, sputtered films are typically in the $\kappa \ll 1$ (low DMI) regime, wherein the field evolution of skyrmions is reminiscent of magnetic bubbles[1–3,15]. Theoretical efforts to bridge these two regimes have prompted a polarising debate on "skyrmions vs. bubbles" – i.e. whether these regimes represent fundamentally distinct magnetic entities[29,34,35]. An experimental resolution to these issues is challenging, as it requires both an integrated imaging approach and a tunable material platform.

A4. Here we elucidate the evolution of these debated skyrmion characteristics over a wide range of κ on a tunable Co/Pt-based multilayer platform. Combining the use of Lorentz transmission electron mi-

croscopy (L-TEM) and magnetic transmission soft X-ray microscopy (MTXM) allows us to probe complementary textural characteristics that are verified by simulations. We establish – with increasing κ – the emergence of Néel helicity, transition from bubble to compact skyrmion character, and a change in skyrmion formation mechanism. In conjunction with an analytical model, these results provide an experimentally driven microscopic framework for tailoring skyrmion character in multilayer films.

B. HELICITY EVOLUTION

B1. Our work is performed at RT using Co/Pt-based multilayer stacks with out-of-plane (OP) anisotropy, which are established hosts of magnetic textures[36]. While symmetric Co/Pt stacks have negligible DMI, asymmetric stacks, such as (Ir or Ta)/Co/Pt can have sizable interfacial DMI ($D > 1$ mJ/m^2) – relevant to chiral magnetic textures[1–3,37]. The inclusion of Fe – as in Ir/Fe/Co/Pt stacks – enhances the DMI, while D and K_{eff} can be smoothly modulated by the Fe and Co thicknesses[4]. Here we study four samples each comprising 1 nm thick FM layers – identified by their **Fe(x)/Co(y)** composition (Tbl. I, thickness in angstroms in parentheses) – wherein the active stack repeated 14 times to optimize full-field microscopic contrast. Interfacial interactions are progressively introduced and quantified using established techniques[1,2,4], with D_{est} varying over $0 – 2$ mJ/m^2 and K_{eff} over $0.08 – 0.70$ MJ/m^3 (Methods, SM1). Consequently, κ varies over $0 – 1.5$, and provides the requisite range for mapping magnetic texture evolution.

B2. The introduction of interfacial DMI should lead to a measurable change in DW helicity[9,38]. L-TEM imaging – wherein contrast results from the magnetization curl parallel to the electron beam – is particularly sensitive to such changes. For normal beam incidence (zero tilt), a pair of homochiral Bloch DWs should express symmetric contrast about their centre, while Néel DWs should exhibit no contrast as their curl is perpendicular to the beam[39]. Meanwhile, the positions of Néel DWs can be deduced by tilting the sample (Fig. 1a),

whereupon antisymmetric contrast of the domains can be observed[30]. To visualize this evolution, we perform tilt-dependent L-TEM imaging with samples deposited on 20 nm SiO$_x$ membranes (see Methods). For ease of analysis, we use OP magnetic fields ($\mu_0 H$) large enough to ensure adjacency of pairs of DWs. Artefacts due to granularity and membrane waviness are mitigated using a recipe that extracts $\sim$1,000 linecuts across domains imaged over a 5 μm field-of-view (see SM2).

B3. Fig. 1 shows stark differences in tilt-dependent L-TEM results for ^{S}Co(10) and Fe(0)/Co(10). First, ^{S}Co(10) ($D_{\mathrm{est}} \simeq 0$, $\kappa \simeq 0$) shows strong, symmetric contrast at zero tilt (a), with a small antisymmetric component at finite tilt (Fig. 1b,c). This is consistent with Bloch DWs expected for symmetric stacks[40–42]. Micromagnetic simulations performed with ^{S}Co(10) parameters (see Methods) suggest that the Bloch DWs are achiral, i.e. lack fixed handedness (see SM4). In comparison, Fe(0)/Co(10) ($D_{\mathrm{est}} \simeq 1.3$ mJ/m^2, $\kappa \simeq 0.3$) shows no contrast at zero tilt (Fig. 1d). Contrast at finite tilt is consistently antisymmetric – and whose amplitude increases with tilt angle (Fig. 1e,f) – consistent with Néel DWs. The absence of measurable symmetric contrast in Fig. 1d-f suggests that any Bloch component – e.g. due to layer-dependent chirality[31,32] – is too small to be detectable[42]. Micromagnetic simulations for Fe(0)/Co(10) also reflect the limited influence
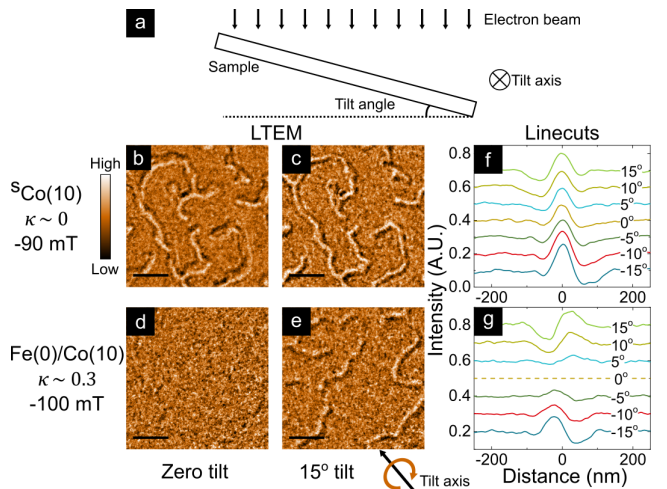

FIG. 1. **DW Helicity from Tilt-Dependent L-TEM Imaging.** (a) Schematic cross-section of L-TEM imaging geometry with sample tilted at angle α with respect to normal incidence of the electron beam. (b-e) Representative L-TEM images (scale bar: 0.5 μm) acquired on samples ^{S}Co(10) (a-b) and Fe(0)/Co(10) (c-d) at $\mu_0 H = 90$ and 100 mT respectively for sample tilts $\alpha = 0°$ (a, c) and $\alpha = 15°$ (b, d). (f-g) Average cross-sectional linecuts across domains detected in L-TEM images of ^{S}Co(10) (f) and Fe(0)/Co(10) (g), with tilt angle α systematically varied over $\pm 20°$. Each curve represents the average of $\sim 1,000$ linecuts extracted from domains imaged over a 5 μm field-of-view using an automated recipe. Dashed vertical lines are expected to be equidistant from the pair of DWs defining the domain.

Acronym	Stack Composition	K_{eff}	D_{est}	κ
^{S}Co(10)	[Pt(10)/Co(10)/Pt(10)]$_{14}$	0.68	0	0
Fe(0)/Co(10)	[Ir(10)/Co(10)/Pt(10)]$_{14}$	0.47	1.3	0.3
Fe(2)/Co(8)	[Ir(10)/Fe(2)/Co(8)/Pt(10)]$_{14}$	0.22	1.8	0.9
Fe(3)/Co(7)	[Ir(10)/Fe(3)/Co(7)/Pt(10)]$_{14}$	0.08	2.0	1.5

Table I. **Sample Compositions.** List of multilayer samples used in this work, with layer thickness in angstroms in parentheses (see Methods, SM1 for full stack details). Corresponding magnetic properties – estimated DMI $D_{\mathbf{est}}$ (mJ/m^2), effective anisotropy $K_{\mathbf{eff}}$ (MJ/m^3) and the stability parameter, κ (dimensionless) – are listed. The samples are henceforth referred to by their **acronym** (left column).

of such layer dependent variations, which are further suppressed if a moderate degree of interlayer coupling is included (see SM4). Finally, similar experiments on the $\kappa \gtrsim 1$ samples produce results fully consistent with Fe(0)/Co(10) (see SM3). Overall, our results indicate that chiral interactions in the $\kappa \sim 0.3$ sample are sufficiently large to transform achiral Bloch textures ($\kappa \simeq 0$) to homochiral Néel textures.

C. COMPRESSIBILITY EVOLUTION

C1. Having established DW helicity evolution, we turn to domain characteristics – which evolve with OP field in addition to magnetic interactions[1,2,4]. Both stripe and skyrmion domains can be collectively characterized by a single length scale, W, defined as domain width of stripes $\simeq$ diameter of skyrmions. Notably, the field-induced variation of W, or dW/dH – termed as **domain compressibility**[43] – should also evolve with κ[4,27,44]. MTXM imaging – wherein dichroic contrast is proportional to local OP magnetization[45] – is well-suited to measure W. Therefore, we performed MTXM imaging with varying OP field using samples deposited on Si_3N_4 membranes, complemented by micromagnetic simulations of hysteresis loops (see Methods). W was determined as an averaged quantity over the full field-of-view using an automated recipe to mitigate granularity effects (see SM2).

C2. Fig. 2 shows MTXM (a-d, i, k) and simulation results (e-g, j, l) of $W(H)$ across samples and presents a striking evolution of behaviour as κ is varied. On one hand, for $\kappa \ll 1$ – illustrated for Fe(0)/Co(10) ($\kappa \sim 0.3$, Fig. 2a-b,i,k) – W shrinks rapidly with field ($\langle dW/dH \rangle \sim 0.5~\mu m/T$, Fig. 2k). Such **highly compressible behaviour** is well reproduced by simulations (Fig. 2e-f), and consistent with the field evolution of "bubble" skyrmions[1–3]. Moreover, the $W(H)$ trend of chiral Néel textures (Fe(0)/Co(10)) is remarkably similar to achiral Bloch textures (^{S}Co(10), Fig. 2h-i). This suggests that for $\kappa \ll 1$, domain compressibility is largely independent of DW helicity. On the other hand, for $\kappa \gtrsim 1$ – shown for Fe(2)/Co(8) ($\kappa \sim 0.9$, Fig. 2c-d,i) – the $W(H)$ variation is much reduced ($\langle dW/dH \rangle \sim 0.1~\mu m/T$, Fig. 2l). Similarly rigid, or incompressible behaviour, is seen for Fe(3)/Co(10) ($\kappa \sim 1.5$), albeit at reduced W, and in analyses of L-TEM images (See SM3). Such incompressibility contrasts sharply with the high compressibility for Fe(0)/Co(10) – despite the helicity, or topology, of the textures being nominally identical. Finally, simulated trends for $\kappa \gtrsim 1$ are also in line with these results (Fig. 2g-h,j,l), suggesting that

it may be understood within a micromagnetic energy framework.

C3. To elucidate the compressibility evolution, we use an analytical model of 1D periodic domains within an infinite magnetic slab of thickness t, domain period λ, and DW width Δ (Figure 3a). The total energy density is given by[34]:
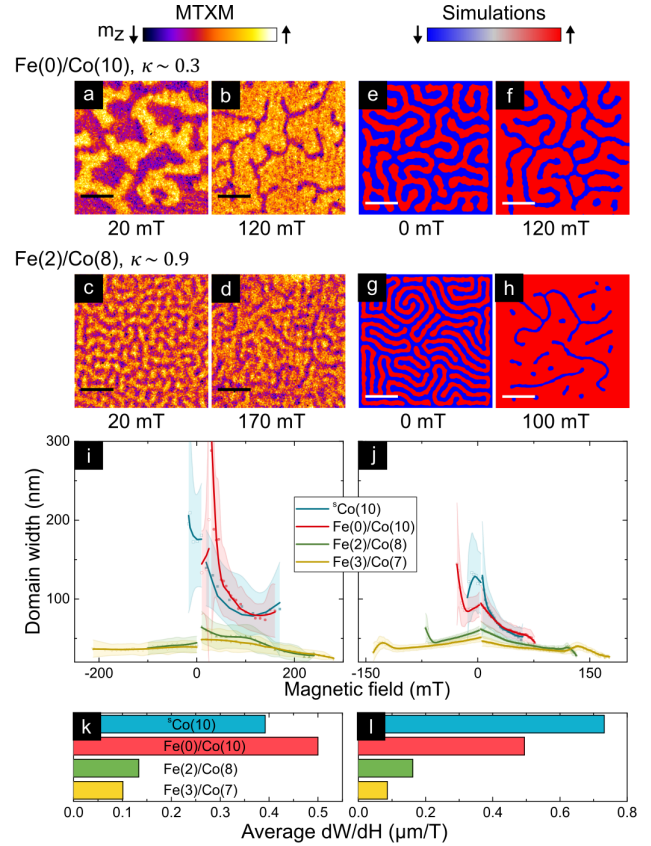

FIG. 2. **Domain Width Field Evolution: MTXM Imaging and Simulations.** **(a-d)** MTXM images of samples Fe(0)/Co(10) ($\kappa \sim 0.3$: a-b) and Fe(2)/Co(8) ($\kappa \sim 0.9$, c-d) – showing domain evolution from near-zero (a,c) to near-saturation (b, d) fields. (scalebar: 0.5 μm) **(e-h)** Simulated magnetization images for magnetic parameters consistent with Fe(0)/Co(10) (e-f) and Fe(2)/Co(8) (g-h) – showing the corresponding evolution from zero (e, g) to higher fields (f, h). **(i-j)** Average minority polarisation domain width, $W(H)$, with varying magnetic field from MTXM experiments (i) and simulations (j) on all four samples studied in this work. Each $W(H)$ data point is a full field-of-view average determined using an automated recipe (See SM2). Solid and open symbols represent magnetization in the negative and positive vertical direction, respectively, and they cross over at the coercive field. Solid lines are guides to the eye. **(k-l)** Magnitude of compressibility, $\langle dW/dH \rangle$, for the four samples from experiments (k) and simulations (j), obtained by extracting the average gradient from (i) and (j) respectively for $\mu_0 H > 0$.

$$\varepsilon_{\text{tot}} = \frac{2}{\lambda}\left[\frac{2A}{\Delta} + 2K_u\Delta + \pi D \sin\psi\right] + \varepsilon_{d,s} + \varepsilon_{d,v} - M_s\left(1 - \frac{2W}{\lambda}\right)B_z, \tag{1}$$

where the magnetostatic energy densities due to surface ($\varepsilon_{d,s}$) and volume charges ($\varepsilon_{d,v}$) are:

$$\varepsilon_{d,s} = \frac{\mu_0 M_s^2}{2}\left(1 - \frac{2W}{\lambda}\right)^2 + \frac{2\pi\mu_0 M_s^2 \Delta^2}{\lambda t}\sum_{n=1}^{\infty}\frac{\sin^2\frac{\pi nW}{\lambda}}{\sinh^2\frac{\pi^2 n\Delta}{\lambda}}\frac{1 - \exp\left(-\frac{2\pi nt}{\lambda}\right)}{n}, \tag{2}$$

$$\varepsilon_{d,v} = \frac{2\pi\mu_0 M_s^2 \Delta^2 \sin^2\psi}{\lambda t}\sum_{n=1}^{\infty}\frac{\sin^2\frac{\pi nW}{\lambda}}{\cosh^2\frac{\pi^2 n\Delta}{\lambda}}\frac{\exp\left(-\frac{2\pi nt}{\lambda}\right) + \frac{2\pi nt}{\lambda} - 1}{n}. \tag{3}$$
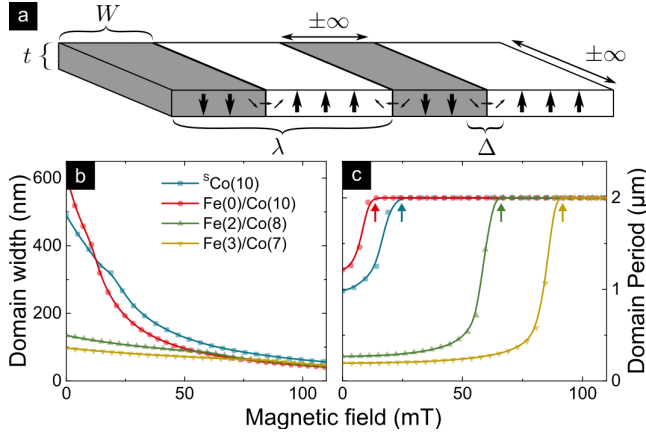

FIG. 3. **1D Model for Domain Compressibility Evolution.** **(a)** Schematic of the simplified analytical model of 1D periodic domains used to interpret the domain compressibility results. Minority domains of wall width Δ, total width W, and period λ are considered in an infinitely long magnetic slab of thickness t and breadth 2 μm. **(b-c)** Field evolution of domain width, $W(H)$ (b, c.f. Fig. 2h-i) and domain period, $\lambda(H)$ (c), obtained from the model (details in text) for magnetic parameters consistent with the samples studied in this work. Arrows in (c) mark the saturation field, H_S, predicted by the model.

C4. The field evolution of W and λ (Fig. 3b-c) are obtained by numerically minimizing ϵ_{tot} with respect to λ, W, and Δ. Notably the 1D model reproduces κ dependence of compressibility noted in experiments (Fig. 2i) and simulations (Fig. 2j): domains are highly compressible for $\kappa \ll 1$, and relatively incompressible for $\kappa \gtrsim 1$. Furthermore, it offers a physical explanation the compressibility evolution when viewed in conjunction with $\lambda(H)$. Within the 1D model, $\lambda(H)$ is indicative of the saturation field, H_S (arrows in Fig. 3c), and the domain density. For $\kappa \gtrsim 1$, wherein H_S is higher (see SM1), domain nucleation occurs just below H_S with smaller size (Fig. 3b) and greater proximity (Fig. 3c). The latter ensures mutual confinement of domains, limiting the expansion of W with reducing H. Therefore, as H is increased from zero, $\kappa \gtrsim 1$ domains have limited latitude for compression, and $W(H)$ is nearly constant – expectedly near the lower cut-off ($W \sim \Delta$). The converse argument holds for $\kappa \ll 1$ domains, which explains their highly compressible $W(H)$ behaviour.

C5. The direct experimental accessibility and consistency with our simulations and 1D model provides compelling justification for compressibility as an important additional classifier of skyrmions. The $\kappa \ll 1$ regime hosts *bubble skyrmions* that are highly compressible with field[1–3]. Here DW formation costs energy and hence skyrmions form when long-range magnetostatic energy contribution is large enough to compensate this cost. In contrast, the $\kappa \gtrsim 1$ regime gives rise to compact skyrmions that are rigid and relatively incompressible[29,35]. In this case, DW formation is energetically favored, which drives their proliferation. Skyrmions may thus form and persist at length scales, $W(H) \sim \Delta$, the DW width. While such classification has been theoretically explored for isolated skyrmions[29,35], our work and provides a firm experimental footing for this yardstick.

D. SKYRMION FORMATION MECHANISM

D1. While skyrmions are known to emerge from stripes with increasing field, the transition may involve one or more mechanisms or paths. Notably, κ, which determines DW stability, is also expected to affect this stripe to skyrmion transition. First, we visually examine the κ-variation of this transition by tracking the simulated field evolution of a prototypical magnetic stripe (details in SM4). We see for $\kappa \sim 0.9$ (Fig. 4a) that the stripe shrinks smoothly with field, and eventually turns into a single skyrmion. Meanwhile, for $\kappa \sim 1.5$ (Fig. 4b), the stripe, abruptly fissions into 4 distinct skyrmions at a characteristic field[46]. These two mechanisms should result in contrasting textural field evolutions that should be detectable in our experiments. Therefore, we statistically examine the field evolution of stripes and skyrmions - distinguished in images by their circularity (See SM2). Here, we choose L-TEM imaging, as it enables a clearer distinction between skyrmions and stripes (See SM2).

D2. Fig. 4c-f present the field evolution of densities of skyrmions (n_S) and stripes (n_R) from L-TEM and simulations for samples Fe(2)/Co(8) and Fe(3)/Co(7). For each case, highlighted regions at intermediate fields – spanning from n_R peak to n_S peak – indicate stripe-to-skyrmion transitions, and exhibit contrasting trends. For Fe(2)/Co(8) ($\kappa \sim 0.9$, Fig. 4c,e) the decrease in n_R ($\sim$2–3 μm^{-2}) corresponds to a one-to-one increase in n_S ($\sim$2–3 μm^{-2}). This is consistent with the shrinking of each stripe to one skyrmion, thereby giving an
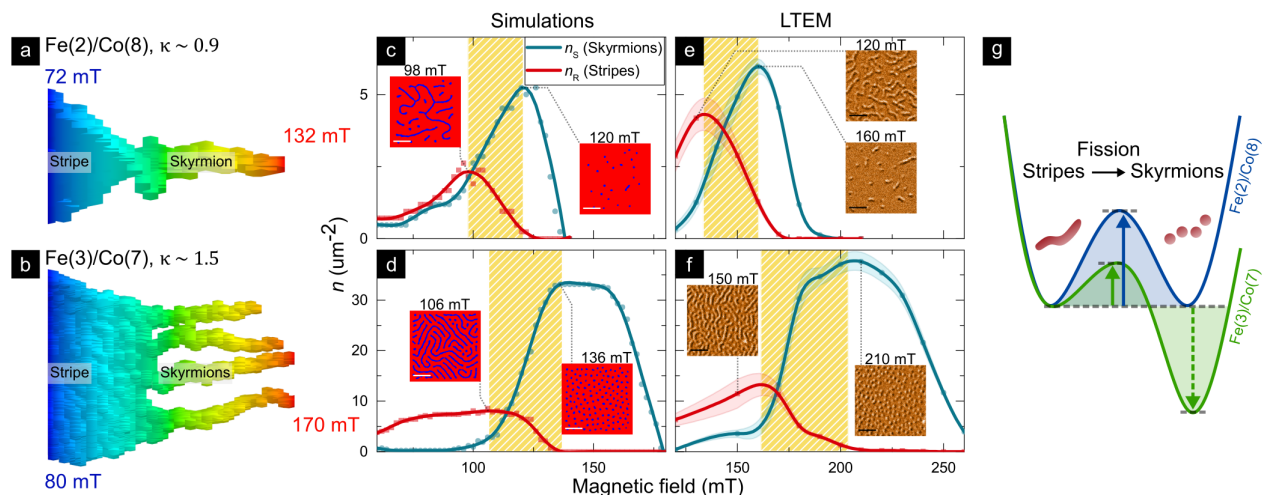
FIG. 4. **Evolution of Skyrmion Formation Mechanism. (a-b)** Simulated field evolution of a prototypical stripe after its separation from the labyrinthine state for (a) Fe(2)/Co(8) ($\kappa \sim 0.9$) and (b) Fe(3)/Co(7) ($\kappa \sim 1.5$) parameters (colorscale indicates field magnitude). The real-space texture is identified and isolated for each field slice and stacked horizontally for comparison. **(c-f)** Field evolution of the density of skyrmions (n_S, teal) and stripes (n_R, red), as extracted from simulations (c-d) and LTEM imaging (e-f) for samples Fe(2)/Co(8) (c, e) and Fe(3)/Co(7) respectively (procedural details in SM2). Highlighted regions denote field ranges corresponding to marked stripe to skyrmion transitions (c.f. a-b). Inset: Simulation and L-TEM images just before and after the transitions (scalebar: 0.5 μm). **(g)** Schematic depiction of the energy landscape governing the fission of stripes into multiple skyrmions for $\kappa \sim 0.9$ (top) and $\kappa \sim 1.5$ (bottom) respectively.

isolated skyrmions (Fig. 4c,e: inset). In contrast, for Fe(3)/Co(7) ($\kappa \sim 1.5$, Fig. 4d,f) the decrease in n_R ($\sim$7-8 μm^{-2}) coincides with a four-fold increase in n_S ($\sim$30 μm^{-2}). This is in line with the fission of each stripe into ~ 4 skyrmions on average, and results in a dense skyrmion lattice (Fig. 4d,f: inset)[46].

D3. The evolution of skyrmion formation mechanism with κ may be understood from energetic and kinetic considerations (Fig. 4g). The fission of a stripe into multiple skyrmions involves DW formation and change in topology. It may occur if energetically favoured and if the associated energy barrier is surmountable[47]. For $\kappa \sim 0.9$, we postulate that the energy saved from DW formation is negligible and the barrier high (Fig. 4g, blue arrow). Therefore, stripes prefer to smoothly shrink into a skyrmion – a process that does not involve an energy barrier. Meanwhile for $\kappa \sim 1.5$, DW formation reduces energy (Fig. 4g, dashed green arrow), favouring the formation of multiple skyrmions. Meanwhile, the associated barrier height (Fig. 4g, solid green arrow) may also reduce with increasing κ – ensuring that fission is the preferred skyrmion formation mechanism.

E. OUTLOOK

E1. In summary, we have elucidated transitions in three critical skyrmion characteristics on a tunable material system using complementary microscopy techniques, supported by simulations and theory. As shown in Fig. 5, these characteristics directly evolve with κ – the material parameter determining chiral DW stability. For $\kappa = 0$, chirality is ill-defined, and ensuing textures have achiral Bloch character, with bubble-

like compressible behaviour. Finite κ enables the formation of Néel DWs with fixed chirality. Round textures observed for $0 < \kappa < 1$ are bubble skyrmions, formed from the shrinking of stripe domains. The Néel DWs enclose a large, uniformly magnetized "core", which makes them highly compressible to external field. Meanwhile, as κ nears unity, DW formation is energetically favoured, and the skyrmions formed are compact, with sizes comparable to Néel DWs. Finally, further increasing κ results in DW proliferation, and skyrmions are now formed in multiplets from the fission of stripes with increasing field.

E2. These insights – established on a single multilayer platform – resolve longstanding issues in the field, and pave new avenues for exploration. Notably, we directly address the polarizing debate on "skyrmions vs. chiral bubbles". Despite their identical topology, these are often labelled as distinct objects and demarcated along material- or size-specific lines. Instead, we have shown that compressibility of chiral skyrmions evolves smoothly with κ – from bubble to compact character – within the same material platform. In fact, compressibility may be an important parameter to tune for skyrmionic devices to balance the counteracting needs of detection (low κ) and stability (high κ). On the theoretical front, we suggest that isolated skyrmion models, while appropriate for certain geometries, may be ably complemented with multi-domain models, as in our case. Meanwhile, the evolution of skyrmion formation mechanism and its efficacy is timely for efforts seeking their stability under near-ambient conditions. Here, our results provide critical material considerations for skyrmion nucleation via spin-orbit torque or

thermally assisted techniques. Finally, spanning the physics of stripes and skyrmions, our work provides a springboard for their use as "skyrmion fabrics" for applications in unconventional computing[19].

F. METHODS

F1. Sample Fabrication. Multilayer films, comprising Ta(40)/Pt(50)/**[HM(10)/Fe(x)/Co(y)/HM(10)]14**/Pt(20) (HM: heavy metal, number in parentheses indicates thickness in angstroms), were deposited by DC magnetron sputtering at room temperature using a Chiron™ UHV system manufactured by Bestec GmbH (base pressure: 10^{-8} Torr). Four samples were studied in this work whose active stack compositions (bolded above) are listed in Tbl. I. To enable direct comparison between different techniques used in this work, the films were simultaneously deposited for magnetometry on thermally oxidized 100 nm Si wafer substrates, for L-TEM on 30 nm-thick SiO_2 membrane windows within Si TEM grids, and for MTXM on 50 – 200 nm thick Si_3N_4 membranes. Magnetometry measurements were performed using a EZ11 vibrating sample magnetometer (VSM) made by MicroSense™. The magnetic parameters: M_S, K_{eff}, A_{est} and D_{est} were obtained using protocols consistent with literature[1,2,4,44], and are detailed in SM1. Notably the interfacial DMI, D_{est} determined for the 14-stack multilayers studied here are in line with measured values on corresponding single stacks from Brillouin light scattering experiments[48].

F2. Lorentz TEM Experiments Lorentz transmission electron microscopy (L-TEM) experiments were performed using an FEI Titan S/TEM operated in Fresnel mode at 300 kV.
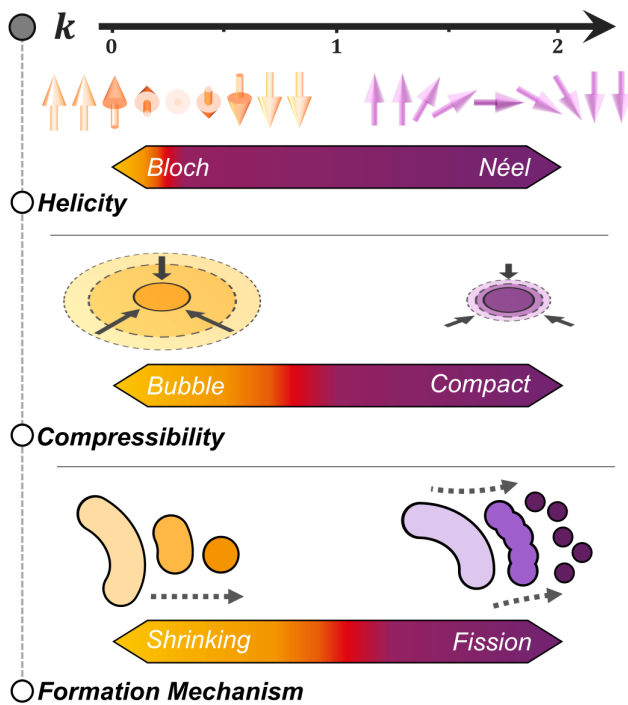
A dedicated Lorentz lens was used for focusing the electron beam. Meanwhile, the objective lens located at the sample position was switched off for imaging acquisition under field-free conditions, or excited to different strengths to apply out-of-plane magnetic fields for in-situ studies of magnetic texture evolution. The applied magnetic field normal to the film plane (from -300 mT to +2 T) was calibrated by placing a Hall probe detector at the sample position. The magnification corresponding to different defocus values were calibrated using a cross-grating replica.

F3. MTXM Experiments. Full-field MTXM imaging experiments were performed using circularly polarised soft x-rays at the Advanced Light Source (XM-1 BL 6.1.2), using the Co L3 edge (∼778 eV) with out-of-plane (OP) sample geometry[49]. OP magnetic fields were applied using an electromagnet, and a pair horse-shoe poles were used to guide the generated flux.

F4. Micromagnetic Simulations. Micromagnetic simulations were performed using mumax[3] to to interpret the field evolution of the 14 repeat multilayer stacks[50]. The simulation field-of-view used was 2 μm × 2 μm, and the cell size was kept to 4 nm × 4 nm × 3 nm, which is below the exchange length for all samples. The effective medium approximation was used with one layer per stack repetition to account for memory constraints[2]. Hysteresis loops were simulated using protocols described in[50].

F5. Image Analysis. Custom-written Python scripts were used for quantitative analysis of magnetic microscopy images. These scripts comprise routines for image filtering and binarization followed by domain characterisation and statistics using standard methods in the scikit-image library[51]. The analysis procedures are detailed in SM2.

FIG. 5. κ-**Driven Evolution of Skyrmion Character.** Overview of the evolution of skyrmion characteristics with increasing κ as seen across the multilayer films studied in this work. This includes the change of DW character (Bloch to Néel), compressibility (bubble to compact), and formation mechanism (shrinking to fission).

* These authors contributed equally to this work.
† anjan@imre.a-star.edu.sg

[1] Moreau-Luchaire, C. *et al.* Additive interfacial chiral interaction in multilayers for stabilization of small individual skyrmions at room temperature. *Nature Nanotechnology* **11**, nnano.2015.313 (2016).

[2] Woo, S. *et al.* Observation of room-temperature magnetic skyrmions and their current-driven dynamics in ultrathin metallic ferromagnets. *Nature Materials* **15**, 501 (2016).

[3] Boulle, O. *et al.* Room-temperature chiral magnetic skyrmions in ultrathin magnetic nanostructures. *Nature Nanotechnology* **11**, 449–454 (2016).

[4] Soumyanarayanan, A. *et al.* Tunable room-temperature magnetic skyrmions in Ir/Fe/Co/Pt multilayers. *Nature Materials* **16**, nmat4934 (2017).

[5] Bobeck, A., Bonyhard, P. & Geusic, J. Magnetic bub-

bles—An emerging new memory technology. *Proceedings of the IEEE* **63**, 1176–1195 (1975).

[6] Baker, K. F. A review of magnetic bubble memories and their applications. *Radio and Electronic Engineer* **51**, 105–115 (1981).

[7] Allwood, D. A. *et al.* Magnetic Domain-Wall Logic. *Science* **309**, 1688–1692 (2005).

[8] Parkin, S. S. P., Hayashi, M. & Thomas, L. Magnetic Domain-Wall Racetrack Memory. *Science* **320**, 190–194 (2008).

[9] Nagaosa, N. & Tokura, Y. Topological properties and dynamics of magnetic skyrmions. *Nature Nanotechnology* **8**, 899 (2013).

[10] Romming, N. *et al.* Writing and Deleting Single Magnetic Skyrmions. *Science* **341**, 636–639 (2013).

[11] Hagemeister, J., Romming, N., von Bergmann, K., Vedmedenko, E. Y. & Wiesendanger, R. Stability of single skyrmionic bits. *Nature Communications* **6**, 8455 (2015).

[12] Kang, W., Huang, Y., Zhang, X., Zhou, Y. & Zhao, W. Skyrmion-Electronics: An Overview and Outlook. *Proceedings of the IEEE* **104**, 2040–2061 (2016).

[13] Tomasello, R. *et al.* A strategy for the design of skyrmion racetrack memories. *Scientific Reports* **4**, 1–7 (2014).

[14] Bhattacharya, D. & Atulasimha, J. Skyrmion-Mediated Voltage-Controlled Switching of Ferromagnets for Reliable and Energy-Efficient Two-Terminal Memory. *ACS Applied Materials & Interfaces* **10**, 17455–17462 (2018).

[15] Jiang, W. *et al.* Blowing magnetic skyrmion bubbles. *Science* **349**, 283–286 (2015).

[16] Lemesh, I. *et al.* Current-Induced Skyrmion Generation through Morphological Thermal Transitions in Chiral Ferromagnetic Heterostructures. *Advanced Materials* **30**, 1805461 (2018).

[17] Büttner, F. *et al.* Field-free deterministic ultrafast creation of magnetic skyrmions by spin–orbit torques. *Nature Nanotechnology* **12**, 1040–1044 (2017).

[18] Woo, S. *et al.* Deterministic creation and deletion of a single magnetic skyrmion observed by direct time-resolved X-ray microscopy. *Nature Electronics* **1**, 288 (2018).

[19] Prychynenko, D. *et al.* Magnetic Skyrmion as a Nonlinear Resistive Element: A Potential Building Block for Reservoir Computing. *Physical Review Applied* **9**, 014034 (2018).

[20] Pinna, D. *et al.* Skyrmion Gas Manipulation for Probabilistic Computing. *Physical Review Applied* **9**, 064018 (2018).

[21] Zázvorka, J. *et al.* Thermal skyrmion diffusion used in a reshuffler device. *Nature Nanotechnology* **14**, 658–661 (2019).

[22] Fert, A., Reyren, N. & Cros, V. Magnetic skyrmions: advances in physics and potential applications. *Nature Reviews Materials* **2**, natrevmats201731 (2017).

[23] Bode, M. *et al.* Chiral magnetic order at surfaces driven by inversion asymmetry. *Nature* **447**, 190 (2007).

[24] Ferriani, P. *et al.* Atomic-Scale Spin Spiral with a Unique Rotational Sense: Mn Monolayer on W(001). *Physical Review Letters* **101**, 027201 (2008).

[25] Bogdanov, A. & Hubert, A. Thermodynamically stable magnetic vortex states in magnetic crystals. *Journal of Magnetism and Magnetic Materials* **138**, 255–269 (1994).

[26] Bogdanov, A. N. & Rößler, U. K. Chiral Symmetry Breaking in Magnetic Thin Films and Multilayers. *Physical Review Letters* **87**, 037203 (2001).

[27] Rohart, S. & Thiaville, A. Skyrmion confinement in ultrathin film nanostructures in the presence of Dzyaloshinskii-Moriya interaction. *Physical Review B* **88**, 184422 (2013).

[28] Leonov, A. O. *et al.* The properties of isolated chiral skyrmions in thin magnetic films. *New Journal of Physics* **18**, 065003 (2016).

[29] Bernand-Mantel, A., Muratov, C. B. & Simon, T. M. Unraveling the role of dipolar versus Dzyaloshinskii-Moriya interactions in stabilizing compact magnetic skyrmions. *Physical Review B* **101**, 045416 (2020).

[30] McVitie, S. *et al.* A transmission electron microscope study of Néel skyrmion magnetic textures in multilayer thin film systems with large interfacial chiral interaction. *Scientific Reports* **8**, 5703 (2018).

[31] Legrand, W. *et al.* Hybrid chiral domain walls and skyrmions in magnetic multilayers. *Science Advances* **4**, eaat0415 (2018).

[32] Dovzhenko, Y. *et al.* Magnetostatic twists in room-temperature skyrmions explored by nitrogen-vacancy center spin texture reconstruction. *Nature Communications* **9**, 1–7 (2018).

[33] Romming, N., Kubetzka, A., Hanneken, C., von Bergmann, K. & Wiesendanger, R. Field-Dependent Size and Shape of Single Magnetic Skyrmions. *Physical Review Letters* **114**, 177203 (2015).

[34] Büttner, F., Lemesh, I. & Beach, G. S. D. Theory of isolated magnetic skyrmions: From fundamentals to room temperature applications. *Scientific Reports* **8**, 4464 (2018).

[35] Bernand-Mantel, A. *et al.* The skyrmion-bubble transition in a ferromagnetic thin film. *SciPost Physics* **4**, 027 (2018).

[36] Belliard, L. *et al.* Stripe domains morphology versus layers thickness in CoPt multilayers. *Journal of Applied Physics* **81**, 5315–5317 (1997).

[37] Fert, A., Cros, V. & Sampaio, J. Skyrmions on the track (2013).

[38] Hellman, F. *et al.* Interface-induced phenomena in magnetism. *Reviews of Modern Physics* **89**, 025006 (2017).

[39] Benitez, M. J. *et al.* Magnetic microscopy and topological stability of homochiral Néel domain walls in a Pt/Co/AlO$_x$ trilayer. *Nature Communications* **6**, 8957 (2015).

[40] Chess, J. J., Montoya, S. A., Fullerton, E. E. & McMorran, B. J. Determination of domain wall chirality using in situ Lorentz transmission electron microscopy. *AIP Advances* **7**, 056807 (2017).

[41] Garlow, J. A. *et al.* Quantification of Mixed Bloch-Néel Topological Spin Textures Stabilized by the Dzyaloshinskii-Moriya Interaction in Co/Pd Multilayers. *Physical Review Letters* **122**, 237201 (2019).

[42] Fallon, K. *et al.* Quantitative imaging of hybrid chiral spin textures in magnetic multilayer systems by Lorentz microscopy. *Physical Review B* **100**, 214431 (2019).

[43] Vernier, N. *et al.* Measurement of magnetization using domain compressibility in CoFeB films with perpendicular anisotropy. *Applied Physics Letters* **104**, 122404 (2014).

[44] Ho, P. *et al.* Geometrically Tailored Skyrmions at Zero Magnetic Field in Multilayered Nanostructures. *Physical Review Applied* **11**, 024064 (2019).

[45] Fischer, P. *et al.* Magnetic imaging with full-field soft X-ray microscopies. *Journal of Electron Spectroscopy and Related Phenomena* **189**, 196–205 (2013).

[46] Tan, A. K. *et al.* Skyrmion Generation from Irreversible Fission of Stripes in Chiral Multilayer Films. *Submitted* (2020).

[47] Desplat, L., Suess, D., Kim, J.-V. & Stamps, R. L. Thermal stability of metastable magnetic skyrmions: Entropic narrowing and significance of internal eigenmodes. *Physical Review B* **98**, 134407 (2018).

[48] Böttcher, T. *et al.* Dzyaloshinskii-Moriya Interaction in Ir/Fe/Co/Pt Stacks: A BLS and DFT Study. *Private Communication* (2020).

[49] Chao, W., Harteneck, B. D., Liddle, J. A., Anderson, E. H. & Attwood, D. T. Soft X-ray microscopy at a spatial resolution better than 15 nm. *Nature* **435**, 1210–1213 (2005).

[50] Vansteenkiste, A. *et al.* The design and verification of MuMax3. *AIP Advances* **4**, 107133 (2014).

[51] Walt, S. v. d. *et al.* scikit-image: image processing in Python. *PeerJ* **2**, e453 (2014).